Separation control in a hypersonic compression ramp interaction

By A.-M. Schreyer†, I. Bermejo-Moreno‡, J. Kim AND J. Urzay

Microramp sub-boundary layer vortex generators minimize the extent of shock-induced separation zones and stabilize shock oscillations, thereby reducing detrimental effects on the performance of high-speed propulsion systems. This study investigates the influence of longitudinal vortices, as introduced by microramps, on a fully separated hypersonic shock-wave/turbulent-boundary-layer interaction. We combine computational and experimental data to provide a framework for detailed investigations of the turbulence structure in complex high-speed compression ramp flows. Large-eddy simulations of two cases corresponding to two experimentally tested conditions are carried out. The first case is a baseline one that consists of a fully separated 33° compression ramp interaction in a Mach-7.2 flow. The second case explores separation control by studying the effect of a row of microramps located upstream of the main compression ramp. The effect of the microramps is represented in the computations by the extra vortex pairs induced in their wakes, which are characterized in isolated microramp simulations and injected in an augmented inflow boundary condition of the main ramp simulations. A dynamic-mode decomposition is applied to the time-resolved numerical data to identify the coherent structures in the baseline and controlled flow fields that are primarily responsible for the characteristics of the separation zones.

1. Introduction

Shock-wave/turbulent-boundary-layer interactions (SWTBLI) occur frequently in the flow field around a hypersonic vehicle. Strong shock waves can induce large-scale separation, causing flow distortion and a significant loss of total pressure. In addition, unsteady effects associated with separated SWTBLI can cause high temperatures and large pressure loads on the vehicle structure (Dupont *et al.* 2006). Thus, it is of practical importance to develop flow control strategies to reduce or prevent shock-induced separation.

Microramp sub-boundary layer vortex generators have been investigated in earlier work on flow control in supersonic engine intakes at Mach numbers below 3.0, see e.g. Anderson *et al.* (2006); Babinsky *et al.* (2009); Blinde *et al.* (2009); Lee (2009). While typically thicker than the viscous sublayer, these microramps are still immersed in the turbulent boundary layer, so that they disturb the outer flow to a lesser extent than conventional vortex generators, causing less drag. Each microramp generates a pair of counter-rotating vortices that entrain high-speed air in the lower regions of the boundary layer, thereby reducing the local displacement thickness (Ford & Babinsky 2007). These vortices break up the two-dimensional separation zone created by the SWTBLI into three-dimensional periodic separation zones (Babinsky *et al.* 2009; Blinde *et al.* 2009; Schreyer *et al.* 2011a), which decreases the separation length (Ford & Babinsky 2007; Babinsky *et al.* 2009) and stabilizes the shock oscillations (Ford & Babinsky 2007).

† Technical University of Braunschweig, Germany
‡ Aerospace and Mechanical Engineering Department, University of Southern California

The relatively low Mach numbers investigated in previous work are far from aerodynamic regimes relevant for hypersonic transportation systems envisioned to provide access to low Earth orbits. Higher Mach numbers of order 7, more relevant to those systems, were experimentally investigated by Schreyer *et al.* (2011a) in a study that included separation control of a compression-ramp interaction by using microramps.

The current study builds on that experimental work by investigating the flow characteristics induced by microramps using large-eddy simulations (LES). The time-resolved LES data are employed to understand the influence of longitudinal vortices induced by the microramps on (1) the spatio-temporal dynamics of the low-frequency shock oscillations, (2) the related breathing motions of the separation bubble, and on (3) the evolution of the vortices shed from the reattachment region. LES results are examined using a dynamic-mode decomposition (DMD), which provides optimal phase-averaged structures corresponding to particular frequencies (Schmid 2010). DMD has been previously applied to SWTBLI flows (Grilli *et al.* 2015; Nichols *et al.* 2016).

The report is organized as follows. The configuration and computational approach are outlined in Section 2. Mean and turbulent flow data from LES, including comparisons with experiments, are presented in Section 3. Descriptions of preliminary results of the DMD analysis are given in Section 4. Ongoing work on this project is described in Section 5. Lastly, conclusions are provided in Section 6.

2. Experimental configuration and computational setup

2.1. *Experimental configuration*

The case investigated in this report matches the geometry and flow conditions of the experiments described in Schreyer *et al.* (2011a,b), which were carried out in the Mach-8 Hypersonic Boundary Layer Facility (HyperBLaF) at the Princeton Gas Dynamics Laboratory. The experimental conditions correspond to a Mach number $\mathrm{M} = 7.2$ and a Reynolds number $\mathrm{Re}_\theta = 3500$ based on the momentum thickness θ at location $x = -20\,\mathrm{mm}$ (see Figure 1) on the flat-plate model without the compression ramp. The embedded model consists of a 30 mm long 33° compression ramp followed by an expansion corner with the same deflection angle, as sketched in Figure 1. The ramp is mounted on a flat plate 350 mm and 151 mm long in the streamwise and spanwise directions, respectively. A trip wire (2.4 mm high) mounted 59 mm downstream of the leading edge of the flat plate causes transition to turbulence, thereby warranting a fully developed turbulent boundary layer in the vicinity of the ramp corner. The undisturbed boundary layer thickness is $\delta_0 = 9.8\,\mathrm{mm}$ at a location 20 mm upstream of the location of the ramp corner. In the flow experiments subject to control of the ramp interactions, seven sub-boundary layer microramps were arranged in a double-row, staggered array and positioned 101.6 mm ($\approx 10\delta$) upstream of the compression corner, as shown in Figure 1. The maximum height h of the microramps is $h = 0.51\delta_0$, with an angle of incidence of 24°. Additional dimensions of the microramps and their spanwise arrangement are described in Anderson *et al.* (2006). In particular, $c/h = 7.2$ and $s/h = 7.5$, where c is the chord length and s is the spanwise spacing between microramps. The streamwise spacing between the two rows of microramps equals the microramp length $l = 32.9\,\mathrm{mm}$.

2.2. *Computational setup*

Wall-resolved LES are performed using the unstructured finite-volume code CharLES^x developed at CTR, which integrates the filtered conservation equations of mass, mo-

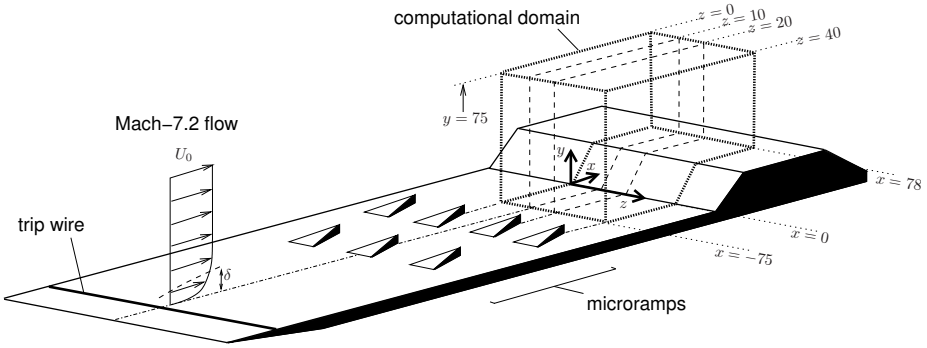

FIGURE 1. Experimental geometry (see Schreyer *et al.* (2011a) for further details) with the LES computational domain and relevant spanwise-normal planes. Distances in mm.

mentum and total energy for a calorically perfect gas using a finite-volume formulation on unstructured hexahedral meshes. The solver is second-order accurate in space and combines a centered numerical scheme away from flow discontinuities with an essentially non-oscillatory (ENO) shock-capturing scheme. Shock waves are identified by a sensor based on local dilatation, enstrophy and sound speed. A three-stage, third-order explicit Runge-Kutta algorithm is used to advance the equations in time. Subgrid-scale (SGS) stresses are modeled following Vreman (2004), with a constant turbulent Prandtl of 0.9 used for the calculation of the SGS heat flux. SGS terms are set to zero in regions marked by the shock sensor, following Bermejo-Moreno *et al.* (2010).

Spanwise periodicity is imposed in the simulation to reduce the computational cost. The spanwise length of the computational domain is $4.1\delta_0$, found in earlier work (Touber & Sandham 2009) to be sufficient to avoid spurious effects on the size of the separation bubble. Confinement effects from side walls, observed to play an important role in SWT-BLI (Bermejo-Moreno *et al.* 2014), are not considered in our present simulations. The inflow plane of the simulations is located 75 mm upstream of the foot of the compression ramp ($x = 0$) and 26.6 mm downstream of the second row of microramps in the experimental configuration. An outflow characteristic boundary condition is used at $x = 78$ mm. Synthetic turbulence is generated at the inflow using a digital filtering technique (Touber & Sandham 2009), requiring mean velocities and Reynolds stresses. These are obtained from experimental particle image velocimetry (PIV) wall-normal profiles at the spanwise center of the baseline configuration by Schreyer *et al.* (2011a,b). The pressure is assumed uniform at the inflow plane and equal to the wall-pressure value $1,366$ Pa measured experimentally. The mean temperature profile in the wall-normal direction is inferred from the mean streamwise velocity profile using Crocco-Busemann's relation with a recovery factor of 0.89. Integral length scales (characterizing two-point correlations) on the inflow plane are taken as δ_0 in the streamwise direction and $\delta_0/2$ in the transverse direction. The integral time scale introduced at the inflow by the synthetic turbulent generator is of the order δ_0/U_0, with $U_0 = 1146$ m/s the free-stream velocity.

The effect of the microramps is modeled by a modified inflow boundary condition, which mimics the resulting vortex pairs in their wakes, assuming that the flow in that region is decoupled from the influence of the compression ramp downstream (see Section 5 for additional simulations that are currently underway that include the microramps in the computational domain). PIV measurements by Sun *et al.* (2012) of a Mach-2 flow past a single microramp of height $h = 5$ mm, geometrically identical to those in Schreyer *et al.*

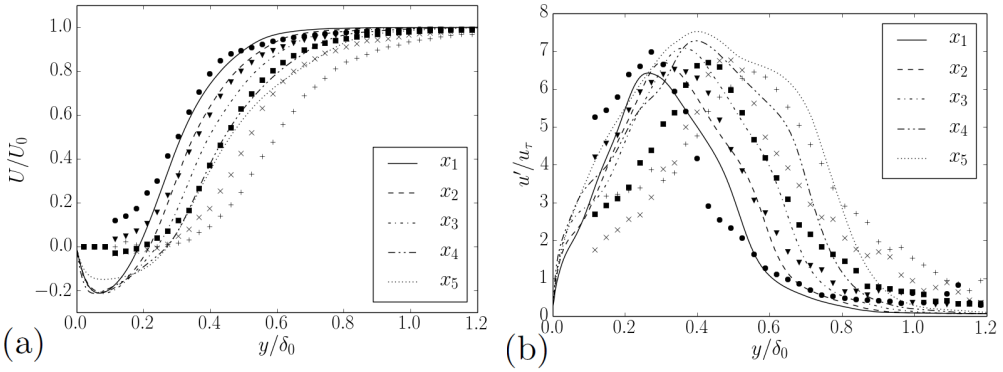

FIGURE 2. LES (lines) and PIV (symbols) mean (a) and rms (b) streamwise velocity profiles at $x-$locations along the interaction for the baseline configuration, where $x_1 = -20\,\text{mm}$ (solid lines and circles), $x_2 = -15\,\text{mm}$ (dashed and triangles), $x_3 = -10\,\text{mm}$ (dash-dotted and diamonds), $x_4 = -5\,\text{mm}$ (dash-dot-dot and diagonal crosses), $x_5 = 0\,\text{mm}$ (dotted and pluses). The free stream velocity $U_0 = 1146\,\text{m/s}$ and the friction velocity $u_\tau = 57\,\text{m/s}$ from the experiment are used to normalize U and u', respectively.

(2011a), are utilized to reconstruct the inflow by rescaling the mean velocity and blending it with the background inflow used in the simulation of the baseline configuration. The effects of the microramps on the boundary layer structure and on the shock-induced separation zone are similar over a wide range of Mach numbers, as observed by comparing the surface flow visualizations in Schreyer *et al.* (2011a), Ford & Babinsky (2007) and Saad *et al.* (2012).

The grid spacings used in the present simulations in the streamwise and spanwise directions are $\Delta x^+ = 40$ and $\Delta z^+ = 20$, respectively. In the wall-normal direction, the grid spacing Δy^+ varies smoothly from 1 at the wall to 5 at $y/\delta_0 = 1.5$. In this notation, the superindex $^+$ refers to viscous units. The resulting grid size is approximately 5 million cells. A constant time step $\Delta t = 5 \cdot 10^{-9}\,\text{s}$ is used for the time integration to facilitate analyses in a frequency domain. The baseline configuration is integrated for a simulation time of 0.25 ms, whereas the microramp-controlled configuration was integrated in time for 2.77 ms, corresponding to approximately 2 and 21 flow-through times, respectively.

3. Mean and fluctuating flow fields

A comparison between PIV and LES for the baseline configuration is shown in Figure 2 for the mean and root-mean-square (rms) streamwise velocities (time- and spanwise-averaged) at different $x-$locations. Although there is qualitative agreement between computations and experiments in the mean velocity profiles, the LES data increasingly deviate from PIV near the compression corner. Additionally, a recirculation region with negative mean streamwise velocities is predicted by the LES at all measurement locations (Figure 2(a)), which is not captured in the PIV. Nonetheless, a separation region was visually observed in surface flow visualizations. This deficiency is attributed in Schreyer *et al.* (2011a) to a possible lack of PIV resolution in the near-wall region, caused by the difficulty to obtain sufficient seeding densities in such strongly separated zones in hypersonic flow.

The effect of the microramps in the controlled configuration is shown in Figure 3, where the contours of mean (time-averaged) streamwise velocity are provided on multiple

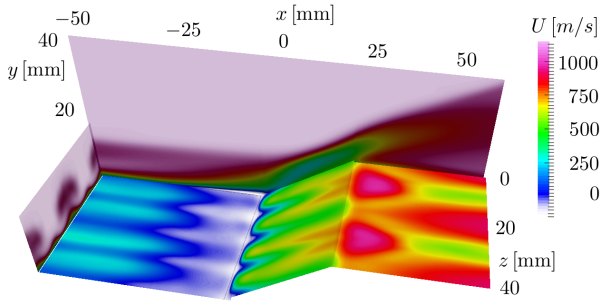

FIGURE 3. Three-dimensional view of contours of mean streamwise velocity mapped onto slices extracted from the simulation of the controlled configuration: transverse (streamwise-normal) plane at $x = -50$ mm, wall-parallel (at 0.1 mm above the horizontal and compression ramp walls) and spanwise-normal at $z \approx 0$.

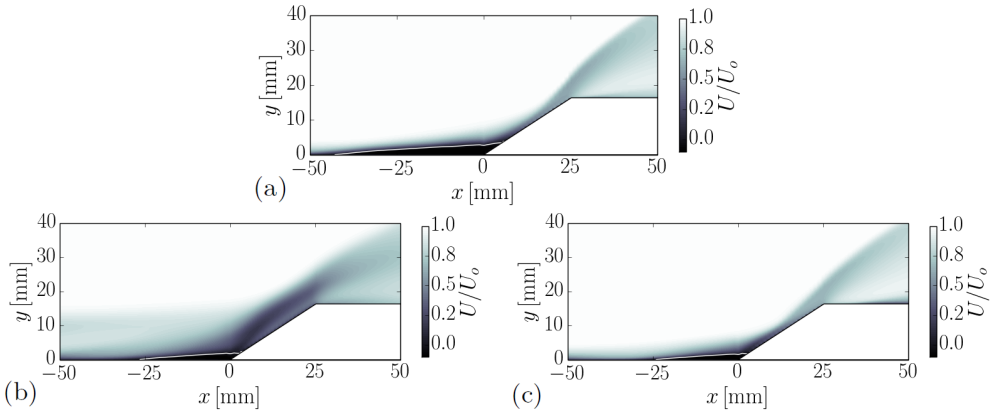

FIGURE 4. Contours of normalized mean streamwise velocity U/U_0 from the baseline simulation (a), and the controlled configuration at (b) $z = 20$ mm and (c) $z = 10$ mm. The solid white line encloses the separation bubble.

planes of a portion of the computational domain (refer to online version for color contour plots). Vortex pairs from the microramps, introduced at the inflow $x = -75$ mm, persist far downstream and interact with the separation zone. Figure 3 shows that the vortex pairs induce a zigzag pattern of streamwise velocity streaks that have a characteristic transverse length equal to one half of the spanwise microramp spacing. These streaks penetrate in the separation zone, breaking the two-dimensional structure found in the baseline case, as also observed in experiments (Schreyer *et al.* 2011a). Figure 4 compares contours of mean streamwise velocity extracted from spanwise-averaging the baseline-case simulation (panel (a)) with those extracted from the controlled-case simulation at the center plane, $z = 20$ mm (panel (b)), which is the symmetry plane of the central microramp in the controlled case, and also at the plane $z = 10$ mm (panel (c)) located half way between the symmetry planes of two consecutive microramps. The velocity streaks induced by the vortex pairs in the controlled case drastically reduce the size of the separation zone, compared with the baseline flow shown in Figure 4(a). The flow over the compression ramp differs significantly between planes $z = 10$ mm and $z = 20$ mm for the controlled case, which is in good agreement with experiments (Schreyer *et al.* 2011a). Downstream of the expansion corner, the pattern of streaks is significantly altered.

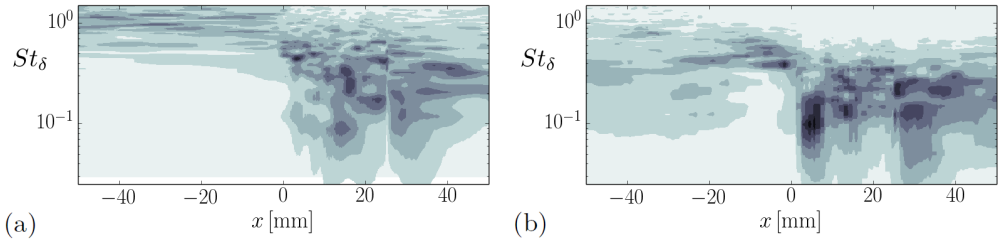

FIGURE 5. Power spectral density of wall-pressure signals extracted along the spanwise center plane ($z = 20\,\text{mm}$) for (a) baseline and (b) controlled cases. Arbitrary logarithmic scale, from white (minimum) to black (maximum).

The effect of the microramps is also noticeable in the wall-pressure dynamics. Specifically, Figure 5 shows premultiplied power spectral densities of wall-pressure time signals for baseline and controlled flow simulations as a function of the streamwise position x and the Strouhal number $\text{St}_\delta = f\delta_0/U_0$, where f is the frequency. The sampling frequency of the wall-pressure signals is given by $\text{St}_\delta = 17$. For the baseline case, results are from an earlier simulation carried out during the Summer Program that is coarser in y but has an integration time comparable to that of the controlled case. Differences between the two spectra are clearly observed. In particular, the turbulent boundary layer upstream of the interaction shows a broader frequency content in the controlled case due to the pressure fluctuations induced by the vortices shed from the microramps. Longer integration time is required to resolve the characteristic low-frequency motions with $\text{St}_\delta = O(0.01)$ typically observed for configurations similar to those of the baseline case (Dupont *et al.* 2006) and to evaluate whether the low-frequency dynamics are modified by the microramps.

4. DMD analysis

Further insight into the dynamics of flow structures can be gained by using DMD (Schmid 2010; Jovanovic *et al.* 2014). This technique enables the extraction of modes and frequencies of dynamical significance, projecting large-scale flow problems onto a modeled dynamical system (i.e., a set of spatial modes) with fewer degrees of freedom. In this study, a sequence of LES time-resolved streamwise velocity fields is analyzed using sparsity-promoting DMD to address the influence of the microramps on the interaction region and on the dominant large-scale coherent structures. The algorithm is applied to instantaneous snapshots extracted from the simulations at multiple planes for different purposes: the streamwise wall-normal planes $z = 10\,\text{mm}$ and $z = 20\,\text{mm}$ to investigate the interaction in the separation region (see Figure 1), and the wall-parallel plane $y = 0.26\delta_0$ to analyze the spanwise structures. The corresponding results are shown in Figures 6-8. The subdomain used for the DMD analysis is the same as that shown in Figure 3. A series of 341 snapshots equi-spaced 7.5 μs in time are analyzed for each case, which render Strouhal numbers in the range $\text{St}_\delta = f\delta_0/U_0 = 0.0067 - 0.57$. Additional simulations are under way that are integrated for longer times in order to provide a more accurate analysis of the low-frequency dynamics.

Figure 6 shows examples of typical DMD mode shapes based on the streamwise velocity component in the center plane ($z = 20\,\text{mm}$) for three selected frequency ranges: the low-frequency range in Figure 6(a,b) where shock oscillation and breathing motion of the separation bubble are commonly found (preliminary); the medium-frequency range in

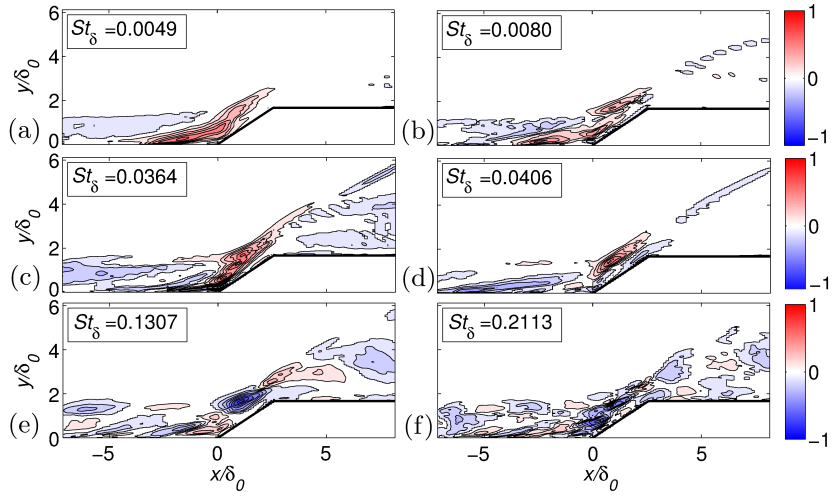

FIGURE 6. DMD modes (real part) on the center plane (controlled flow case) for Strouhal numbers St_δ of (a) 0.0049, (b) 0.0080, (c) 0.0364, (d) 0.0406, (e) 0.1307, (f) 0.2113.

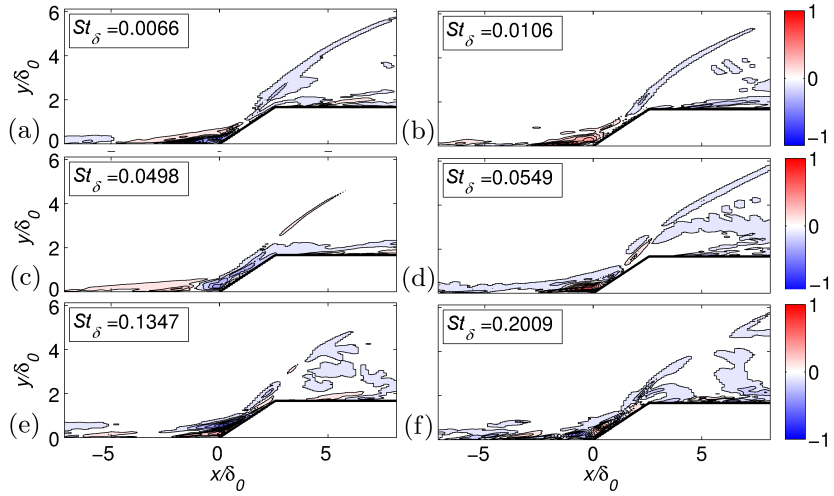

FIGURE 7. DMD modes (real part) on the $z = 10\,\mathrm{mm}$ plane for the controlled flow case for Strouhal numbers St_δ of (a) 0.0066, (b) 0.0106, (c) 0.0498, (d) 0.0549, (e) 0.1347, and (f) 0.2009.

Figure 6(c,d) corresponding to characteristic modes of shock motion induced by the interaction with large-scale vortices passing through the shock (Ringuette *et al.* 2006); and the high-frequency range in Figure 6(e,f) typical of vortical structures in the shear layer. The color scale is normalized with the maximum amplitude. Most of the energy in these dominant modes is contained in the separation bubble and shear layer. Structures in the incoming boundary layer also show a significant energy content, as described above in the context of the wall-pressure signals shown in Figure 5. This extra energy content is not usually observed in undisturbed SWTBLI (e.g., see Nichols *et al.* (2016)) and may be attributed to the wakes from the microramps. In fact, DMD modes computed on the plane $z = 10\,\mathrm{mm}$, located between two of the vortex pairs induced by the microramps,

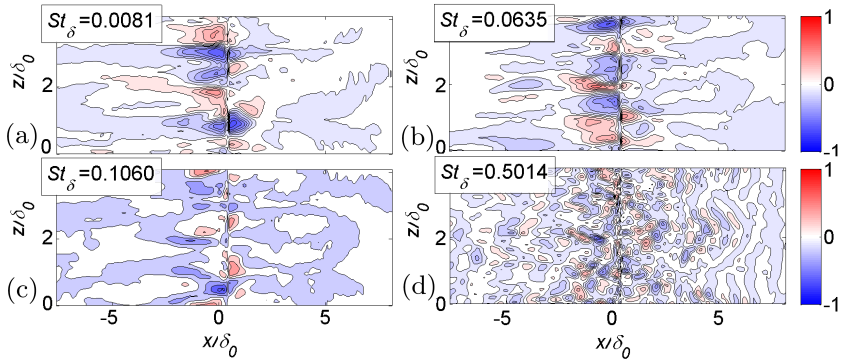

FIGURE 8. DMD modes (real part) on the wall-parallel plane $y = 0.26\delta_0$ for the controlled flow case for Strouhal numbers St_δ of (a) 0.0081, (b) 0.0635, (c) 0.1060, and (d) 0.5014.

support this assumption, since much less energy is contained in the incoming boundary layer along that plane, as observed in Figure 7.

Dynamic modes computed on the wall-parallel plane in Figure 8 reveal a transverse instability in the separation zone that was also observed in the baseline case, and therefore cannot be solely attributed to the microramp-induced vortices. Possible sources of this instability may be the spanwise rippling of the shock due to passing coherent structures (Ringuette *et al.* 2006), or Görtler vortices created by the ramp concavity, which here are found to have a spanwise spacing of approximately $1\delta_0$ in agreement with the findings of Dawson & Lele (2015). However, elucidation of these aspects in the present flow configurations requires further research.

5. Ongoing work

Additional simulations in larger computational domains are currently pursued. These are aimed at capturing the complete dynamics by including a two-row array of microramps in a computational domain of 5.8 million cells in a fully coupled configuration similar to the experimental setup of Schreyer *et al.* (2011a). Local grid adaption is applied to selectively refine the grid. A baseline simulation without the microramps in the same computational domain with 3.7 million cells is also run for comparison purposes. The resulting instantaneous velocity contours at the center plane $z = 20\,\mathrm{mm}$ are shown in Figure 9(a,b). Similarly, statistics of the streamwise velocity profiles at $x = -20\,\mathrm{mm}$ are provided in Figure 9(c,d). This augmented dataset will be used for detailed inspection of the interactions of the separation bubble with the wakes generated by the microramps.

6. Conclusions

In this study, we have investigated the influence of longitudinal vortices, as introduced by a row of three sub-boundary layer microramps, on a fully separated hypersonic SWT-BLI created by a 33° main compression ramp in a Mach-7.2 flow. Two experimentally tested configurations by Schreyer *et al.* (2011a), corresponding to a baseline case without microramps and a controlled flow case including microramps, have been numerically simulated using LES. The effect of the microramps is modeled by modifying the inflow boundary condition. Qualitative agreement between LES and PIV data of Schreyer *et al.* (2011a) was found for both configurations. The effect of the microramps is observed to

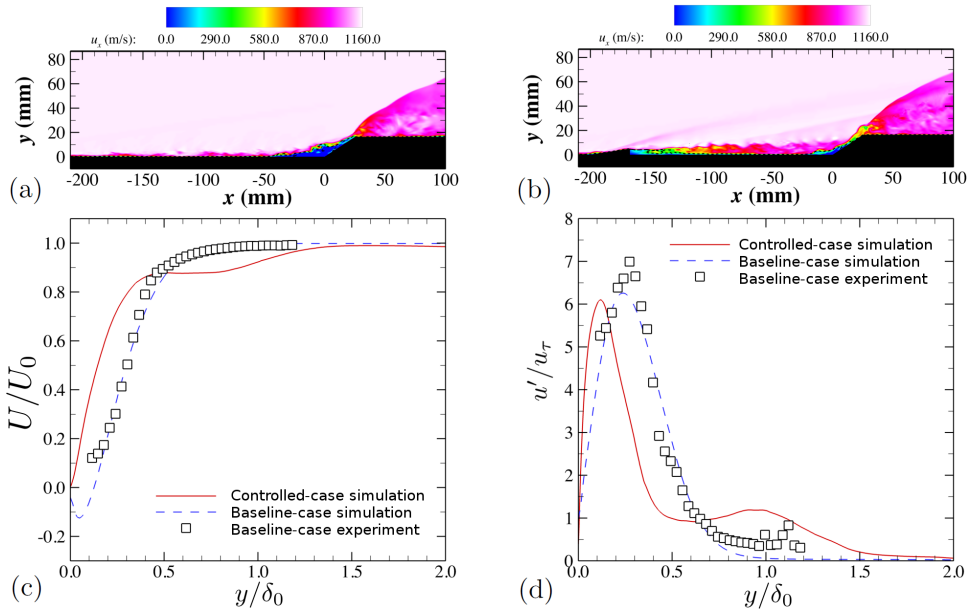

FIGURE 9. Instantaneous contours of streamwise velocity at the center plane $z = 20$ mm for (a) baseline and (b) controlled flow configurations. Wall-normal profiles of (c) time-averaged and (d) rms streamwise velocity at $x = 20$ mm upstream of the ramp corner are also shown, with symbols indicating the experiments of Schreyer *et al.* (2011a)

reduce the size of the separation bubble with respect to the baseline case. The size reduction in the controlled flow case is caused by the generation of a zigzag pattern of the separation line upstream of the compression ramp that breaks the spanwise homogeneity. As a result, wall-pressure time signals show a broader spectrum of frequencies in the incoming boundary layer in the controlled flow configuration. DMD analyses of instantaneous streamwise velocity fields revealed the dominant flow structures associated with different frequency ranges. A transverse mode instability in the separation zone is also educed from the DMD analysis in both baseline and controlled flow configurations. The influence of the microramps on the low-frequency motions characteristic of SWTBLI is currently under investigation.

Acknowledgments

The authors acknowledge use of computational resources from the Certainty cluster awarded by the National Science Foundation to CTR. Fruitful discussions during the Summer Program with S. Lele, P. Schmid and R. Pecnik are gratefully acknowledged.

REFERENCES

ANDERSON, B. H., TINAPPLE, J. & SURBER, L. 2006 Optimal control of shock wave turbulent boundary layer interactions using micro-array actuation. *AIAA Paper* 2006-3197.

BABINSKY, H., LI, Y. & FORD, C. W. P. 2009 Microramp control of supersonic oblique shock-wave/boundary-layer interactions. *AIAA J.* **47**, 668–675.

BERMEJO-MORENO, I., LARSSON, J. & LELE, S. K. 2010 LES of canonical shock-

turbulence interaction. *Annual Research Briefs*, Center for Turbulence Research, Stanford University, pp. 209–222.

Bermejo-Moreno, I., Campo, L., Larsson, J., Bodart, J., Helmer, D. & Eaton, J. K. 2014 Confinement effects in shock wave/turbulent boundary layer interactions through wall-modeled large-eddy simulations. *J. Fluid Mech.* **758**, 5–62.

Blinde, P. L., Humble, R. A., van Oudheusden, B. W. & Scarano, F. 2009 Effects of micro-ramps on a shock-wave/turbulent boundary layer interaction. *Shock Waves* **19**, 507–520.

Dawson, D. M. & Lele, S. K. 2015 LES of a three-dimensional compression ramp shock-turbulent boundary layer interaction. *AIAA Paper* 2015-1518

Dupont, P., Haddad, C. & Debive, J.-F. 2006 Space and time organization in a shock-induced separated boundary layer. *J. Fluid Mech.* **559**, 255–277.

Ford, C. W. P. & Babinsky, H. 2007 Micro-ramp control for oblique shock wave/boundary layer interactions. *AIAA Paper* 2007-4115.

Grilli, M., Schmid, P. J., Hickel, S. & Adams, N. 2012 Analysis of unsteady behaviour in shockwave turbulent boundary layer interaction. *J. Fluid Mech.* **700**, 16–28.

Jovanovic, M. R., Schmid, P. J. & Nichols, J. W. 2014 Sparsity-promoting dynamic mode decomposition. *Phys. Fluids* **26**, 024103.

Lee, S. 2009 *Simulation of shock boundary layer interaction control using micro-vortex generators.* Ph.D. Thesis, University of Illinois at Urbana Champaign.

Nichols, J. W., Larsson, J., Bernardini, M. & Pirozzoli, S. 2016 Stability and modal analysis of STBLIs. *Theor. Comput. Fluid Dyn.* (In Press).

Ringuette, M. J., Martin, M. P., Smits, A. J. & Wu, M. 2006 Characterization of the turbulence structure in supersonic boundary layers using DNS data. *AIAA Paper* 2006-3539.

Saad, M. R., Zare-Behtash, H., Che-Idris, A. & Kontis, K. 2012 Micro-ramps for hypersonic flow control. *Micromachines* **3**, 364–378.

Schmid, P. J. 2010 Dynamic mode decomposition of numerical and experimental data. *J. Fluid Mech.* **656**, 5–28.

Schreyer, A.-M., Sahoo, D. & Smits, A. J. 2011a Experiments on the influence of a microramp array on a hypersonic shock turbulent boundary layer interaction. *AIAA Paper* 2011-3428.

Schreyer, A.-M., Sahoo, D. & Smits, A. J. 2011b Turbulence measurements with PIV in a hypersonic shock/boundary layer interaction. *AIAA Paper* 2011-3429.

Sun, Z., Schrijer, F. F. J., Scarano, F. & van Oudheusden, B. W. 2012 The three-dimensional flow organization past a micro-ramp in a supersonic boundary layer. *Phys. Fluids* **2**, 055105.

Touber, E. & Sandham, N. 2009 LES of low-frequency unsteadiness in a turbulent shock-induced separation bubble. *Theor. Comput. Fluid Dyn.* **23**, 79–107.

Vreman, A. W. 2004 An eddy-viscosity subgrid-scale model for turbulent shear flow: Algebraic theory and applications. *Phys. Fluids* **16**, 3670–3681.